

Interface nanocavities in poly (lactic acid) membranes with dispersed cellulose nanofibrils: Their role in the gas barrier performances

M. Dickmann^{a,b,*}, S. Tarter^c, W. Egger^a, A. Pegoretti^d, D. Rigotti^d, R.S. Brusa^{c,e}, R. Checchetto^c

^a Institut für Angewandte Physik und Messtechnik LRT2, Universität der Bundeswehr München, Werner-Heisenberg-Weg 39, 85577, Neubiberg, Germany

^b Heinz Maier Leibnitz Zentrum (MLZ), Technische Universität München, Lichtenbergstraße 1, 85748, Garching, Germany

^c Department of Physics, University of Trento, Via Sommarive 14, 38123, Povo, Trento, Italy

^d Department of Industrial Engineering, University of Trento, Via Sommarive 9, 38123, Povo, Trento, Italy

^e TIFPA/INFN, Via Sommarive 14, 38123, Povo, Trento, Italy

ARTICLE INFO

Keywords:

Poly (lactic acid)
Bio-nanocomposites
Functionalized nanocellulose
Gas barrier
Interface nanocavities
Positronium

ABSTRACT

Poly (lactic acid) nanocomposites containing lauryl-functionalized cellulose nanoparticles were prepared by solution-casting method and structurally characterized. The gas transport process was studied in $\sim 50 \mu\text{m}$ thick nanocomposite films with filler contents up to 12 vol% using He, $^2\text{H}_2$, N_2 and CO_2 as test gases. The gas permeability and diffusivity was evaluated by studying the permeation process using a specific mass spectroscopy technique in the temperature range from 298 K to 340 K in transient and stationary transport conditions. We present original diffusivity and permeability data as a function of the temperature together with the obtained values for the activation energy. Gas transport data were correlated with information on the nanocomposite free volume structure obtained by positron annihilation lifetime spectroscopy. The results indicate that the decrease of the gas barrier performances observed in nanocomposites with filler contents larger than $\sim 5 \text{ vol}\%$ is due to an increased gas solubility caused by the formation of rigid cavities at the interface between the polymer matrix and micrometer-sized filler aggregations.

1. Introduction

Bioplastics obtained from sustainable natural resources such as corn-derived poly (lactic acid) (PLA), microorganism-derived polyhydroxy alkanates (PHA) and polyhydroxy butyrate (PHB) are biodegradable materials. They widely studied as promising substitution candidates for ethylene vinyl alcohol (EVOH) or polyvinylidene chloride (PVDC), which are commercial petroleum-derived polymers used as gas barrier layers for packaging applications [1]. Presently, PLA is increasingly used for packaging of fresh food products given by its biodegradable nature. However, its thermal, mechanical and gas barrier properties are far from the standards required for other commercial uses [2]. The preparation of PLA nanocomposites, i.e. the dispersion of filler nanoparticles in a biopolymer matrix is a common approach to obtain enhanced material properties [3–6].

Nanocellulose is a bio-based nanostructure obtained from plants or microorganisms. Its application as a filler particle in PLA would permit

the synthesis of a fully biodegradable material. It can be prepared as crystalline nanorods, generally called nanocellulose crystals (NCC), or as nanofibrils (NCF) with both, crystalline and amorphous regions [7].

Using nanocellulose as a filler particle is driven by the exceptional mechanical properties, optical transparency [7] as well as its gas-impermeable nature. Furthermore, chains of macromolecular cellulose form a dense network due to strong hydrogen bonding [8–10]. To enhance the nanocellulose dispersion degree in the hydrophobic PLA matrix, some kind of surface functionalization is required, since nanocellulose fibrils exhibit high polarity and are, thus, poorly compatible with PLA [11]. Different functionalization routes have been explored as, for example, grafting with monomers [11], silylation [12], acetylation [13] or esterification [14].

In a previous paper, we reported a study on the preparation and characterization of PLA nanocomposites containing up to 16.6 vol% of nanocellulose particles, esterified by lauryl chains (LNC) [15]. The gas transport tests through $\sim 50 \mu\text{m}$ thick nanocomposite films were carried

* Corresponding author. Institut für Angewandte Physik und Messtechnik LRT2, Universität der Bundeswehr München, Werner-Heisenberg-Weg 39, 85577, Neubiberg, Germany.

E-mail address: marcel.dickmann@unibw.de (M. Dickmann).

<https://doi.org/10.1016/j.polymer.2020.122729>

Received 16 May 2020; Received in revised form 10 June 2020; Accepted 12 June 2020

Available online 15 June 2020

0032-3861/© 2020 Elsevier Ltd. All rights reserved.

out at 310 K only. The results evidenced a non-monotonic variation of the gas barrier properties with the content of dispersed nanocellulose [LNC] [15]. Initially, the gas permeability P decreased by adding LNC filler particles, reaching a value of $P = 70\%$ lower than for neat PLA at a critical filler content $\sim 5\text{ vol}\%$ (6.5 wt%). By a further increase of the filler particle concentration, the gas permeability progressively grew. It reached the value of the neat PLA film at [LNC] $\sim 12\text{ vol}\%$. Furthermore, we also observed that the penetrant diffusivity D did not significantly change adding filler particles, which evidences that tortuosity effects on the penetrant diffusivity play a minor role in the gas transport process. This trend was observed with test gases of different molecular size and condensation properties. Structural analysis revealed that an increase of [LNC] does not influence thermal properties of the PLA matrix like the melting point and the glass transition temperature. Also the fraction between crystalline and amorphous regions remains constant [15]. However, we found different types of structures for nanocomposites with various filler content by scanning electron microscopy. Cross-sectional images revealed, in fact, that nanocellulose particles disperse completely inside the PLA matrix up to contents of [LNC] $\sim 5\text{ vol}\%$. By increasing [LNC] the filler particles start forming micrometer-sized, spherical-shaped agglomerates. Given by the gas-impermeable nature of the LNC particles and the absence of structural effects on the PLA matrix, we correlated the gas barrier performances of the nanocomposite with structural modifications of the interface layers between PLA and the dispersed/aggregated nanocellulose [16].

For the analysis of the permeability data we applied equations obtained from models for gas transport through Mixed Matrix Membranes (MMM) with defected interfaces, see Ref. [17] For a detailed review. We used these models in previous investigations on the gas transport properties of graphene-based polymer nanocomposites [18,19]. The nanocomposite permeability is evaluated modelling the nanocomposite as a continuous polymer phase with a dispersed pseudo-phase consisting of the filler particle surrounded by a defected polymer interface layer. Such defects can be interface nano-voids, formed when the polymer chains do not wet the filler particles, or they can be rigidified polymer layers, which are formed when macromolecular chains are well adherent to the filler particles [20]. The nanocomposite effective permeability was evaluated using the ideal Maxwell model [21] first to describe the permeability of the pseudo-phase, later to calculate the effective permeability of the nanocomposite [16,17,19,21].

We explained the improved gas barrier performances for well dispersed filler particles by the formation of rigidified PLA layers in the close environment of the functionalized nanocellulose particles. The used models suggest for these regions an effective thickness between 8 and 10 nm, which is comparable to the length of the lauryl chains [15, 16]. The progressive loss of the gas barrier performances for higher concentrations of filler particles was, on the contrary, attributed to the formation of PLA regions around the LNC precipitates, more permeable for the migrating gases than the neat PLA matrix. Assuming an operative hypothesis that precipitates are formed only by the LNC particles in excess to [LNC]_c $\sim 5\text{ vol}\%$, the MMM models suggested an effective thickness in the micrometer range for these more permeable interface regions [15,16].

Driven by the strong applicative interest for this 100%-biodegradable material obtained from renewable resources, we present in this paper a study with the goal to gain a deeper understanding on the mechanisms controlling the gas transport through PLA-LNC nanocomposites.

To this task we carried out gas phase permeation experiments in a wide temperature range on the neat PLA film and on the nanocomposite with critical LNC concentration, assumed as reference materials to analyze the microscopic processes controlling the gas transport in nanocomposites where PLA precipitation occurs. In addition to the previously studied penetrants (CO₂, N₂ and ²H₂), we also used He, a penetrant molecule of smaller size. The obtained mass transport

information was correlated to the free volume structure of the nanocomposite, experimentally investigated by Positron Annihilation Lifetime Spectroscopy (PALS) [22].

2. Experimental section

2.1. Nanocomposite preparation and their microstructural analysis

Detailed information of the preparation and functionalization of the cellulose nanocrystals and on the preparation of pure and nanocomposite thin films are reported in Refs. [15].

Briefly, poly(lactic acid) was purchased from Nature Works LLC (1.24 g/cm³ mass density, 160 °C melting point) while high purity cellulose was obtained from commercial bags of hydrophilic cotton. The nanocellulose was prepared according to the following procedure: 150 ml of 40% sulphuric acid and 5 g of cellulose were stirred for 1 h at 50 °C; a sodium carbonate solution was used to neutralize the resulting solid and subsequently washed with tetrahydrofuran and dried in vacuum. The bio-additive functionalization was carried out according to this procedure: nanocellulose fibers (1 g) and lauryl chloride (11.5 ml) were mixed with 15 ml toluene and 4.1 ml pyridine. The mixture was heated at 80 °C and precipitated by the addition of 400 ml ethanol. To remove pyridine and lauryl chloride excess, the product was washed with ethanol and dried under vacuum.

PLA-LNC films were prepared by solution mixing and casting. PLA was dissolved in chloroform (CHCl₃) under magnetic stirring at 40 °C. Functionalized nano-cellulose was dispersed in chloroform and sonicated at a power of 200 W in an ice bath. The PLA-CHCl₃ and LNC-CHCl₃ solutions were then mixed with a magnetic stirrer for 3 h. The obtained solutions were casted in a Petri dish. After solvent evaporation, first at room temperature for 24 h and then in a ventilated oven at 40 °C for 4 h, nanocomposite films of $\sim 50\ \mu\text{m}$ thickness were obtained and stored in a desiccator filled with silica gel.

TEM measurements revealed that the dimensions of LNC nanostructures in the PLA matrix are between 400 and 500 nm long with a mean radius of $r_d \sim 10\text{ nm}$ [16]. We know also from cross-sectional SEM micrographs that the LNC filler particles are completely dispersed inside the PLA matrix and form sub-micrometer sized agglomerates, if the filler content does not exceed a critical concentration of [LNC]_c $\sim 5\text{ vol}\%$. At larger concentrations the filler particles precipitate by producing agglomerates with nearly spherical shapes of sizes between $\sim 0.8\ \mu\text{m}$ at 5.4 vol% to $\sim 1.4\ \mu\text{m}$ at $\sim 10\text{ vol}\%$ content. The glass transition temperature T_g , the melting temperature T_m and the fraction of crystalline PLA structures X_c were obtained by Differential Scanning Calorimetry (DSC). The results show that the values for T_g and T_m of the PLA matrix ($331 \pm 1\text{ K}$ and $439 \pm 1\text{ K}$, respectively) are not changed by adding filler particles. The crystalline fraction X_c slightly decreased from 2.3 vol% in the neat PLA sample to 1.2 vol% in the nanocomposites [15].

2.2. Gas transport tests

The gas transport properties of the nanocomposite membrane samples were studied by gas phase permeation technique using a home-made apparatus described in Ref. [23]. Transport tests were carried out with PLA-LNC nanocomposite samples, cut as thin discs of diameter $d = 13.5 \pm 0.1\text{ mm}$ and thickness $L \sim 50\ \mu\text{m}$ in a temperatures range between 298 and 338 K using high purity and dry test gases He, ²H₂, CO₂ and N₂. At time $t = 0$, one side of the membrane was exposed to the test gas at a fixed feed gas pressure p_{feed} . Gas molecules are absorbed by the membrane surface layers, diffuse through the inner membrane layers and reach the other membrane side. This side faces a steadily pumped UHV chamber. Here, desorbed molecules form a rarefied gas in thermal equilibrium with the chamber walls at temperature T_{ch} . The partial gas pressure $p(t)$ increases with time t and reaches, after a transient interval time, a constant value \hat{p} , indicating that stationary transport conditions

(*stc*) are set [23]. The $p(t)$ signal provides, in continuous pumping conditions, a measure of the test gas permeation flux $j(t)$ according to the relation $j(t) = \frac{S_p}{R \cdot A \cdot T_{ch}} p(t)$ where S_p is the pumping speed of the vacuum system, R the universal gas constant and A the membrane surface area [23]. In our experimental apparatus the partial pressure of the permeating test gas, $p(t)$, was measured, as a function of time t , using a calibrated Quadrupole Mass Spectrometer (QMS, QMG 420 Balzers).

2.3. Positron annihilation lifetime spectroscopy (PALS)

We used PALS to investigate the free volume inside the membranes, i. e. the size and distribution of cavities and intrinsic nano-holes. This technique is a well-established for the characterization of polymers in material science [24]. All measurements were performed using the Pulsed Low-Energy Positron System (PLEPS) [25,26], an instrument for depth-resolved PALS at the research reactor FRM II. PLEPS pulses the continuous, mono-energetic positron beam of the intense source NEPOMUC [27,28] and enables, therefore, positron lifetime measurements with high acquisition rates. The final kinetic beam energy can be tuned between 0.25 and 20 keV. Since the probability to implant a positron deeper into the sample increases with its energy, we are able to vary the mean implantation depth \bar{z} by adjusting the implantation energy. In general, the implantation profile is strongly correlated to the material properties and can be described as a Makhovian function [29]. By averaging this function, one obtains \bar{z} as:

$$\bar{z} = \frac{A}{\rho} E^n \quad (1)$$

The parameters ρ and E represent the material density and the positron implantation energy in units of keV, respectively. A and n are material dependent constants, which have been found experimentally in several previous investigations, e.g. for polymers in Ref. [30]. For all measurements we chose a positron implantation energy of 16 keV so that the beam reached a mean implantation depth of $\bar{z} = 2.4 \mu\text{m}$ ($A = 2.8 \mu\text{g} \cdot \text{cm}^{-2} \cdot \text{keV}^{-n}$, $n = 1.7$, $\rho = 1.24 \text{ g/cm}^3$).

The positron beam is focused by a magnetic lens onto the sample and reaches a circular shaped spot of about 1 mm (FWHM) on the membrane surface. The annihilation radiation was received with a BaF₂ scintillator detector, magnetically shielded and protected from radiation arising from backscattered positrons. In combination with the pulsing components of PLEPS we reached an overall time resolution of ≈ 180 ps. All samples were measure under high-vacuum conditions ($< 10^{-8}$ mbar) and at 5 different temperatures between 308 and 353 K. After the highest temperature was reached, the samples were cooled down and measured again at the initial temperature of $T = 308$ K. For each spectrum more than 4 million counts were collected.

A spectrum $Z(t)$ obtained with PLEPS includes a sum of lifetime terms, where each term includes an individual lifetime component τ_i and intensity I_i . In the raw spectra, this sum of terms is convoluted with the instrument resolution function $R(t)$ and added by a constant background:

$$Z(t) = R(t) \otimes \left[\sum \frac{I_i}{\tau_i} \exp\left(-\frac{t}{\tau_i}\right) \right] + \text{Background} \quad (2)$$

To analyze the measured data, the resolution function $R(t)$ is determined by a numerical deconvolution of a spectrum deriving from a reference sample (*p*-doped silicon carbide) with well-known lifetime components, measured at the same implantation energy [22].

For the investigation of free volume inside polymers the following process is important. After implantation a positron can form a bound state with an electron, called positronium (*Ps*). *Ps* is formed likely in open volumes and at the surfaces and exists in two configurations with respect to the total spin: *para-*Ps** (spin = 0) and *ortho-*Ps** (spin = 1). Because of the invariance of charge conjugation the binding particles of *ortho-*Ps** cannot annihilate directly in two gamma rays of 511 keV which

leads to different lifetimes for both states. *Para-*Ps** annihilates into two gamma rays with a vacuum lifetime of $\tau_{para} = 125$ ps, while *ortho-*Ps** annihilates into three gamma rays with a vacuum lifetime of $\tau_{ortho} = 142$ ns. When *ortho-*Ps** is formed in an open volume inside a material like holes in polymers, its lifetime is reduced to few nanoseconds due to the pick-off process, where the positron annihilates favorably with an electron of the medium with opposite spin. This happens when *ortho-*Ps** interacts with the wall of the open volume in which it is formed. Assuming spherical shaped holes the correlation between radius R and τ_{ortho} is described by the semi-empiric, quantum mechanical Tao-Eldrup model [31,32]:

$$\tau_{ortho} = \frac{1}{2} \left[1 - \frac{R}{R + \Delta R} + \frac{1}{2\pi} \sin\left(\frac{2\pi R}{R + \Delta R}\right) \right]^{-1} [\text{ns}] \quad (3)$$

The parameter $\Delta R = 1.656 \text{ \AA}$ is an empirically found value, which represents the overlap of the *ortho-*Ps** wave function with the material around the hole, modelled as a potential well [33]. To obtain τ_{ortho} we analyzed the measured lifetime spectra with a numerical fitting routine using the program *PalsFit3* [34].

3. Results

3.1. Gas transport through neat PLA films

In Fig. 1 we present the experimental $j(t)$ curves for a $49 \pm 1 \mu\text{m}$ thick neat PLA film at 310 K exposed to the four test gases at feed gas pressure $p_{feed} = 40$ kPa. These curves show an initial transient time interval where $j(t)$ increases with time t followed by stationary transport conditions, where $j(t)$ exhibits a time-constant value. The $j(t)$ curves were fitted with the function:

$$J(t) = J_{stc} \left[1 + 2 \sum_{n=1}^{\infty} (-1)^n \exp\left(-\frac{D n^2 \pi^2 t}{L^2}\right) \right] \quad (4)$$

which describes, in the framework of the solution-diffusion model [35], the kinetics of the permeation flux through a membrane film of thickness L exposed to a permeant gas kept at pressure p_{feed} . Here, $J_{stc} = \frac{D \cdot S}{L} p_{feed}$ is the permeation flux in stationary transport conditions. The model assumes that the rate-limiting parameters are the penetrant diffusivity D and solubility S in the membrane layers.

Measuring the gas permeation flux value in stationary transport conditions $\hat{j} = \frac{S_p}{R \cdot A \cdot T_{ch}} \hat{p}$ permits to evaluate the membrane gas permeability $P = D \cdot S$ by the relation $j_{stc} = \frac{D \cdot S}{L} p_{feed}$, where the feed gas pressure p_{feed} and the sample thickness L are known parameters. The gas

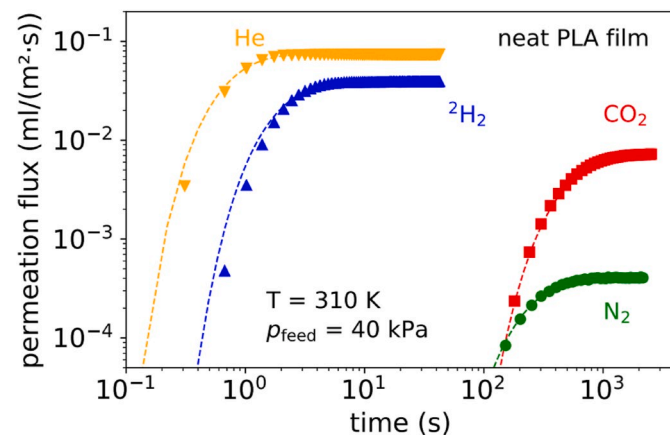


Fig. 1. Permeation curves obtained at 310 K with a $49 \pm 1 \mu\text{m}$ thick neat PLA film. Experimental data are plotted as markers, while dashed lines represent the data fitting, obtained in the framework of the solution-diffusion model (Eq. (4)) [35]. Experimental indeterminations are within the size of the symbols.

diffusivity D can be obtained by fitting the $j(t)$ curves. The Arrhenius plot of the carbon dioxide data for P and D obtained in the temperature range of 298 K – 338 K is presented in Fig. 2.

The activation energy values for permeation E_P and diffusion E_D were obtained fitting the data for P and D the relations:

$$P(T) = P_0 \exp\left(-\frac{E_P}{RT}\right) \quad (5a)$$

$$D(T) = D_0 \exp\left(-\frac{E_D}{RT}\right) \quad (5b)$$

where P_0 and D_0 are temperature independent pre-factors; see dashed lines in Fig. 2 and data in Table 1.

It is suitable to compare our obtained activation energy values for permeation with those obtained by other researchers. Bao et al. obtained in a study of gas transport through amorphous solution-casted poly (98.7% L-lactide) films, with CO_2 and N_2 penetrants, values for E_P of 18.5 ± 0.3 kJ/mol and 34.6 kJ/mol, respectively (PLA was provided by Purac Biochem, Holland) [36]. Auras et al. reported in their review paper slightly lower values for the CO_2 activation energy of permeation: 15.7 kJ/mol for poly (98 % L-lactide) films with 40 % crystallinity and 19 kJ/mol for poly (94 % L-lactide) films with 25 % crystallinity (samples provided by Cargill Dow LLC) [37]. We found in literature only the value for E_D obtained by Bao et al. for CO_2 which is 37 ± 1 kJ/mol [36]. No report was found on the activation energy for the N_2 diffusion or the permeation and diffusion for small-size penetrants like He and $^2\text{H}_2$ through this biopolymer.

3.2. Gas transport through PLA-LNC nanocomposite films

In Fig. 3 we present the experimentally obtained $j(t)$ curves for CO_2 and nanocomposite films with different LNC contents measured at 338 K. The solid markers are pertinent to the pure PLA film, measured at the same temperature. This plot reveals two key points [15]:

- Looking at the permeation flux in stationary transport conditions, we observe that the CO_2 barrier properties of the nanocomposite sample with $[\text{LNC}] = 5.4$ vol% are clearly improved with respect to those of the neat PLA film. By increasing the filler content this improvement gets progressively lost: at $[\text{LNC}] \sim 12$ vol% the permeation flux in stationary transport conditions is nearly equivalent to that of the neat PLA film.
- On the contrary, we find no remarkable differences for the duration between the permeation processes. Thus, we conclude that the

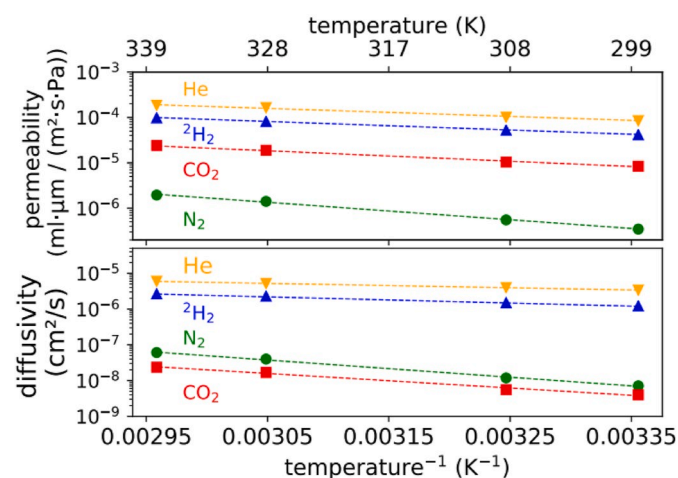


Fig. 2. Arrhenius plot of the gas permeability P and diffusivity D values in the neat PLA film for the examined test gases. Experimental indeterminations are inside the size of the symbols.

Table 1

Activation energy values for permeation (E_P) and diffusion (E_D) of the examined test gases and the neat PLA film.

| | E_P (kJ/mol) | E_D (kJ/mol) |
|----------------|----------------|----------------|
| CO_2 | 22.4 ± 0.8 | 39 ± 2 |
| N_2 | 36.6 ± 0.8 | 46 ± 2 |
| $^2\text{H}_2$ | 18.3 ± 0.8 | 16.5 ± 0.8 |
| He | 17.5 ± 0.8 | 11.7 ± 0.8 |

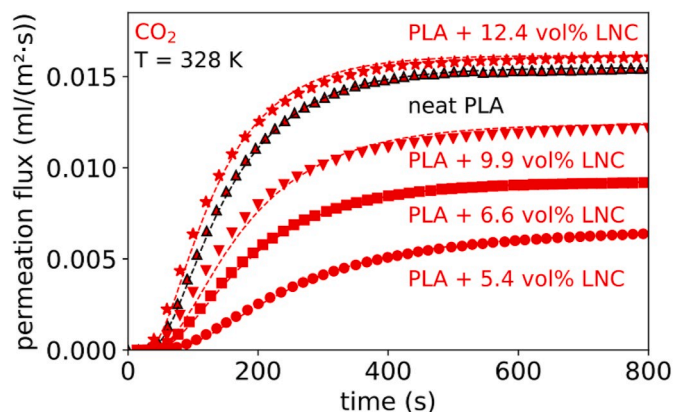


Fig. 3. CO_2 permeation curves of PLA-LNC nanocomposite films with different LNC contents at 328 K. Markers represent the $j(t)$ curve pertinent to the neat PLA sample. Experimental indeterminations are inside the size of the symbols. Dashed lines are fittings of the permeation curves using Eq. (4).

addition of LNC particles has minor influences on the kinetics of the penetrant molecule migration inside the PLA matrix.

Gas transport measurements through the nanocomposites were carried out with all test gases and the obtained $j(t)$ curves (not reported here) show similar behavior. We fitted the $j(t)$ curves to quantitatively describe the two previously discussed performances. The obtained P and D transport parameters are reported in Fig. 4 as a function of the LNC content. The plot reveals that $[\text{LNC}]_c = 5.4$ vol% is a critical filler content for all gases:

- it produces the optimal gas barrier performances and

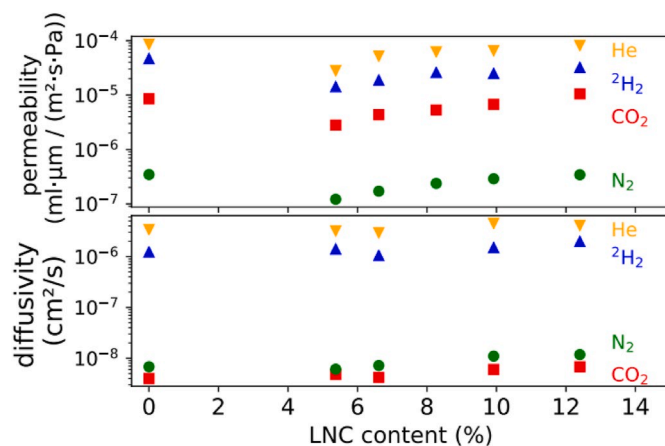


Fig. 4. Gas permeability P and diffusivity D of neat PLA and PLA-LNC nanocomposites as a function of the LNC filler content at $T = 298$ K. (circles/green: N_2 , squares/red: CO_2 , up triangles/blue: $^2\text{H}_2$, down triangles/orange: He). Experimental indeterminations are inside the size of the symbols. (For interpretation of the references to colour in this figure legend, the reader is referred to the Web version of this article.)

ii) for $[LNC] > [LNC]_c$ the gas permeability increases with the LNC content.

It is certain for all test gases that the D value only changes slightly with respect to neat PLA by increasing $[LNC]$.

In Fig. 5 we present Arrhenius plots of the CO_2 permeability P and diffusivity D for nanocomposites of different LNC content. The dashed lines represent fittings of the experimental data using Eqs. (5a) and (5b). We evaluated from these models the activation energy for permeation E_p and diffusion E_D . E_p exhibits its largest value for CO_2 of $E_p = (36 \pm 2)$ kJ/mol in the nanocomposite with $[LNC] = 5.4$ vol%. Then, it progressively decreases adding filler particles and reaches a value of $E_p = (22 \pm 1)$ kJ/mol in the nanocomposite with $[LNC] = 12.4$ vol%, equivalent to the value for neat PLA ($E_p = (22.4 \pm 0.8)$ kJ/mol).

The activation energy for diffusion E_D of CO_2 was (40 ± 2) kJ/mol in all nanocomposites. The value is equivalent, inside the experimental indetermination, to the value obtained with for neat PLA, (39 ± 2) kJ/mol. This trend of E_p and E_D for $[LNC] \geq 5.4$ vol% was observed with all examined test gases, see Table 2.

3.3. Free volume structure

The best fits of the measured PALS spectra were obtained with three lifetime components, where the long lifetime component τ_3 results from the annihilation of *ortho*-Ps (*o*-Ps) confined inside free volume holes of the polymer. Here, τ_3 is of special interest since it can be used to determine the size of the free volume holes. To this task we used Eq. (3) which provides the average value of the hole radius R assuming that holes forming the polymer free volume structure are spherical cavities.

The measured lifetime components τ_3 and the corresponding average hole radius R are presented in Fig. 6 as a function of temperature for nanocomposites with different LNC content. Fig. 6 reveals that at a fixed sample temperature, R increases with the filler content; at a fixed filler content, R increases with the sample temperature. At a temperature of 310 K, for example, the average radius R increases from 0.287 nm in the neat PLA sample to 0.295 nm inside the nanocomposite with $[LNC] = 4.1$ vol% and progressively increases up to 0.302 nm in the nanocomposite with $[LNC] = 9.9$ vol%. Note that the increase of the *ortho*-Ps lifetime evidenced by comparing the neat and the nanocomposite samples cannot be attributed to *ortho*-Ps annihilation processes inside the dispersed or aggregated LNC filler particles. In fact, previous experiments [38] on nanocellulose coatings revealed a much shorter long lifetime component τ_3 of 1.4 ns.

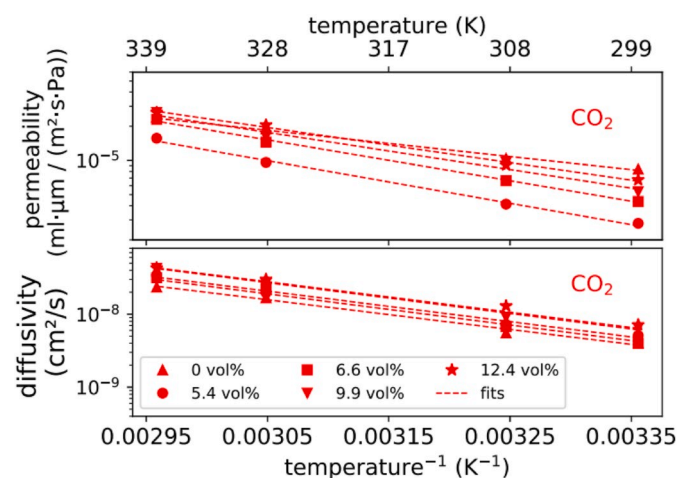


Fig. 5. Arrhenius plot of the CO_2 permeability P and diffusivity D of PLA-LNC nanocomposites with different LNC content. Circles: 5.4 vol%, squares: 6.6 vol%, triangles: 9.9 vol%, stars: 12.4 vol%. Dashed lines are data fits using Eqs. (5a) and (5b).

Table 2

Activation energy values for permeation (E_p) of PLA-LNC nanocomposites for the examined test gases.

| [LNC] (vol%) | CO_2 | N_2 | $^2\text{H}_2$ | He |
|--------------|----------------|----------------|----------------|----------------|
| 0 | 22.4 ± 0.8 | 36.6 ± 0.8 | 18.3 ± 0.8 | 17.5 ± 0.8 |
| 5.4 | 36 ± 2 | 47 ± 2 | 34 ± 1 | 27 ± 1 |
| 6.6 | 34 ± 1 | 45 ± 2 | 32 ± 1 | 21 ± 1 |
| 9.9 | 30 ± 1 | 45 ± 2 | 30 ± 1 | 18 ± 1 |
| 12.4 | 22 ± 1 | 42 ± 2 | 26 ± 1 | 17 ± 1 |

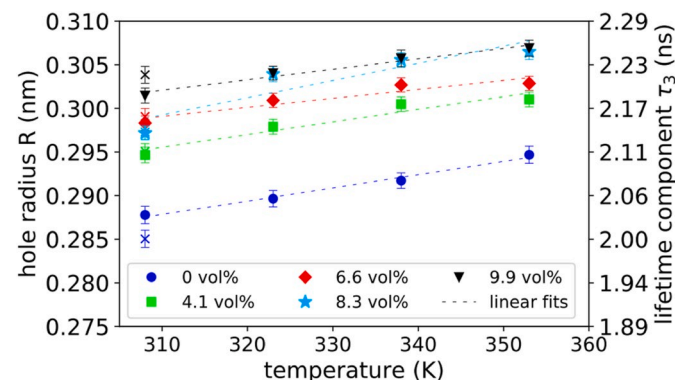


Fig. 6. Average radius R of the free volume holes and corresponding *o*-Ps lifetime value τ_3 measured at different temperatures in nanocomposites samples with different LNC contents. Dashed lines are linear fits of the experimental data. Data points marked with an X are measured after cooling down from 353 K to 309 K and are not used for the linear fits.

A linear fit of the average R values as a function of temperature for the neat PLA sample and the different nanocomposites reveals, inside the experimental indetermination, equal slope values of $dR/dT = (1.52 \pm 0.12) \cdot 10^{-4}$ nm/K.

This can be explained by the fact that the introduction of LNC particles creates additional open volumes at the interface region between filler and PLA matrix, whereby these volumes are larger than the free volumes holes inside the PLA matrix and only insignificantly affected by the temperature. The formation of such rigid cavities is in agreement with the fact that we did not observe any change in the thermal properties of the nanocomposites nor in the effective value of the activation energy for diffusion of all penetrants changing the filler content.

The intensity plot of Fig. 7 shows that a higher amount of LNC content, up to 8.3 vol%, increases I_3 . This points to a generation of new open volumes. However, the sample with the highest amount of $[LNC]$ (9.9 vol%) shows an *o*-Ps intensity inferior than the sample with $[LNC] = 8.3$ vol%.

This can be explained by the fact that an increase of the LNC content also increases the sizes of the agglomerates so that the surface region, where the open volumes are formed, decreases. The decrease in intensity with temperature (Fig. 7) can be ascribed to two different effects: The first is the combination or disappearance of some open volumes in the interfacial regions. The second effect is the modification of the PLA matrix due to the loss of residual CHCl_3 solvent molecules after heating [16,39], as observed with thermal desorption measurements. In fact, in all the samples, we obtain different values for τ_3 and I_3 , after cooling down from $T = 353$ K – 308 K, indicating a change in the PLA matrix.

The fractional free volume f_h of the neat and nanocomposite samples can be evaluated by the relation $f_h = C \cdot V \cdot I_3$ [40] where $V = \frac{4}{3} \pi R^3$ is the average hole volume and C is a coefficient that depends on the polymer chemistry, related to the probability of *ortho*-Ps formation inside its holes. In order to compare f_h values of pure and nanocomposite samples it is necessary to consider the different amount of LNC content in each nanocomposite and rescale the measured I_3 value according to the

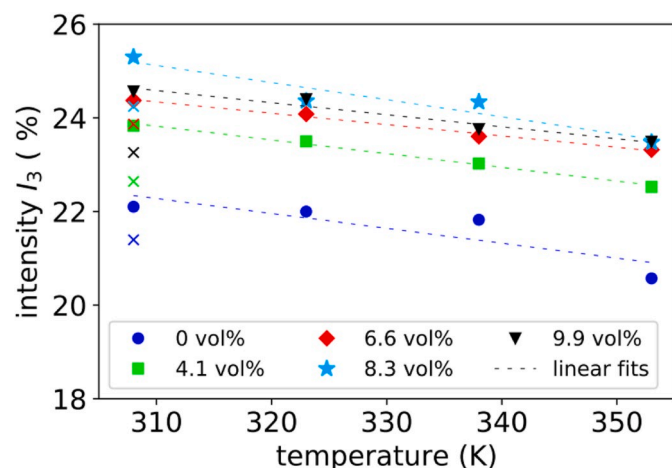


Fig. 7. Intensity I_3 of the *o*-Ps annihilation signal at different temperatures in PLA-LNC nanocomposites with different LNC content. Dashed lines are linear fit of the experimental data. Data points marked with x are pertinent to samples cooled to 309 K after their heating at 353 K.

relation $I_3 = \frac{1}{1-x} \cdot I_3$, where x is the volume fraction occupied by the filler particles in the nanocomposite. Moreover, since the parameter C is not known, we evaluate the $f_{h,rel}$ value of each nanocomposite with respect to that of the neat PLA sample, which we thus consider as reference material: $f_{h,rel} = f_h(\text{nanocomposite})/f_h(\text{neat})$. The $f_{h,rel}$ quantities are reported in Fig. 8 which indicates that $f_{h,rel}$ increases slightly up to 338 K and then decreases at higher temperatures.

The $f_{h,rel}$ quantity is a function of the parameters I_3 and τ_3 , which change with temperature in opposite directions (see Figs. 6 and 7). The $f_{h,rel}$ growth is thus driven by the thermal expansion of the free volume holes up to 338 K. Afterwards it is dominated by I_3 as shown by the fact that $f_{h,rel}$ decreases. After heating and cooling down the samples to $T = 308$ K, the hole sizes shrunk more or less to their initial values at 308 K, however some of them vanished. Therefore, also the fractional free volume has changed in an irreversible way. We observe this behavior for all samples, even for pure PLA, which is an indication that the change of the material structure is related to partial solvent desorption from the PLA matrix.

3.4. Correlation of interface structure and transport properties

Structural analysis, reported in a previous paper, show that filler

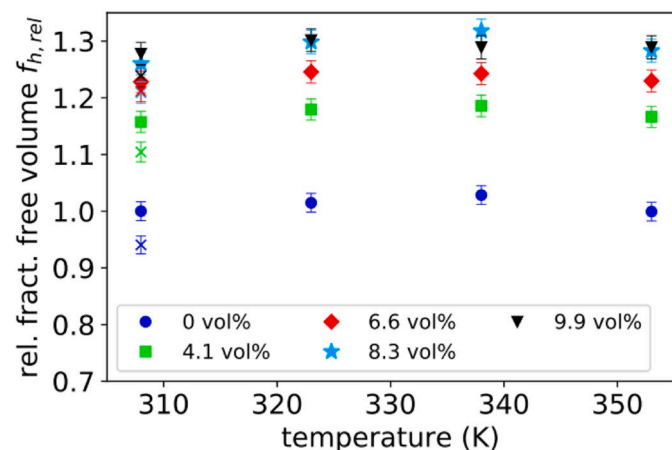


Fig. 8. Relative fractional free volume $f_{h,rel}$ of nanocomposite samples with different LNC content as a function of the temperature. Data points marked with x are measured after sample cooling down from 353 K to 309 K.

contents larger than a critical value of $[LNC] \sim 5$ vol% precipitate, forming nearly spherical agglomerates in the PLA matrix with sizes in the micrometer range: the number of agglomerates, the density as well as their sizes increase with the filler content. The results reported in the previous section on the gas transport through the nanocomposites evidence that the gas permeability P progressively increases when the filler content overcomes this critical value while negligible variation occur in the gas diffusivity values. This trend was observed for all examined temperature and all test gases. The worsening of the nanocomposite gas barrier performances is accompanied by a progressive decrease of the activation energy for gas permeation E_p to the value obtained with the neat PLA film; on the contrary, the effective activation energy for diffusion E_D maintains more or less constant on a similar value to those obtained with the neat PLA film.

Experimental tests have revealed the gas transport process through the present nanocomposites obeys to the solution-diffusion mechanism which predicts that the gas permeability P is given by the product of gas solubility S and gas diffusivity D in the polymer layers. Accordingly, the loss of gas barrier properties is related to an increase of the effective gas solubility S in the polymer layers resulting from the formation of the gas-impermeable LNC filler agglomerates. Note that structural analyses have revealed that the presence of these precipitates did not induce those changes in the structure of the PLA matrix that usually influence its transport properties [41]: in fact, no change was observed either in the glass transition temperature T_g , nor in the crystalline fraction of the PLA matrix [15]. The increase of the gas solubility can be, thus, explained considering that structural variations only occur in the PLA layers surrounding the filler particles resulting from the presence of the rigid cavities, detected by PALS, which are larger in size than the free volume holes distributed in the PLA matrix. These sites increase the effective gas solubility of the nanocomposite acting as supplementary solution sites for the permeating gas molecules. These cavities do not influence the gas transport kinetics, see Fig. 4: these facts clearly indicate that the localized cavities are not interconnected and consequently do not provide additional migration paths for the migrating gas molecules. The filling of these cavities by the permeating gas is controlled by the molecular diffusion process in the matrix PLA layer and, thus, it appears with the same time scale as that of the whole permeation process.

4. Conclusions

We combined experimental information on the thermochemical properties of poly (lactic acid) nanocomposites containing gas-impermeable lauryl functionalized cellulose nanoparticles, with their free volume structures observed by positron annihilation lifetime spectroscopy to elucidate the mechanisms responsible for the loss of gas barrier properties. Results evidence that the filler aggregation process, occurring at LNC contents larger than ~ 5 vol%, induces an increase of the effective gas solubility as observed with test gases, having different molecular size and condensation properties. This effect is a consequence of the formation of PLA layers around the filler agglomerates, which are rigid and have non-interconnected cavities of larger size than the average free volume holes of the PLA matrix. These voids act as additional solution sites for permeating gas molecules. Moreover, original information of the neat PLA and PLA-LNC nanocomposites free volume structure and relevant values of the activation energies for gas permeation and diffusion are reported.

Declaration of competing interest

The authors declare that they have no known competing financial interests or personal relationships that could have appeared to influence the work reported in this paper.

CRedit authorship contribution statement

M. Dickmann: Software, Validation, Formal analysis, Investigation, Data curation, Writing - original draft, Visualization. **S. Tarter:** Formal analysis, Investigation, Validation. **W. Egger:** Investigation, Resources, Supervision, Funding acquisition. **A. Pegoretti:** Writing - review & editing, Resources. **D. Rigotti:** Writing - review & editing, Resources. **R. S. Brusa:** Conceptualization, Writing - review & editing, Supervision, Project administration. **R. Checchetto:** Methodology, Writing - review & editing, Supervision, Formal analysis.

Acknowledgements

We thank Prof. D. Carretti and Prof. M. Rizzuto (University of Bologna, Italy) for providing us functionalized nanocellulose. Parts of this work are based on experiments performed at the NEPOMUC PLEPS instrument, operated by FRM II at the Heinz Maier Leibnitz Zentrum (MLZ), Garching, Germany. Funding from the German BMBF (projects 05K10WNA-Posimethod, 05K13WN1-Posianalyse, 05K16WN1-Positec and 05K19WN1-Posilife) is gratefully acknowledged.

References

- [1] X.Z. Tang, P. Kumar, S. Alavi, K.P. Sandeep, *Crit. Rev. Food Sci. Nutr.* **52** (2012) 426–442, <https://doi.org/10.1080/10408398.2010.500508>.
- [2] M. Jamshidian, E.A. Tehrani, M. Imran, M. Jacquot, S. Desobry, *Compr. Rev. Food Sci. Food Saf.* **9** (2010) 552–571.
- [3] F. Carosio, S. Colonna, A. Fina, G. Ryzdzek, J. Hemmerlé, L. Jierry, P. Schaaf, F. Boulmedais, *Chem. Mater.* **26** 5459–5466.
- [4] J.M. Raquez, Y. Habibi, M. Murariu, P. Dubois, *Prog. Polym. Sci.* **38** (2013) 1504–1542.
- [5] A.J. Svagan, A. Akesson, M. Cardenas, S. Bulut, J.C. Knudsen, J. Risbo, D. Plackett, *Biomacromolecules* **13** (2012) 397–405, <https://doi.org/10.1021/bm201438m>.
- [6] A. Dorigato, M. Sebastiani, A. Pegoretti, L. Fambri, *J. Polym. Environ.* **20** (2012) 713–725, <https://doi.org/10.1007/s10924-012-0425-6>.
- [7] A. Dufresne, *Mater. Today* **16** (2013) 220–227.
- [8] N. Lavoine, I. Desloges, A. Dufresne, J. Bras, *Carbohydr. Polym.* **90** (2012) 735–764, <https://doi.org/10.1016/j.carbpol.2012.05.026>.
- [9] S.S. Nair, H. Chen, Y. Peng, Y. Huang, N. Yan, *ACS Sustain. Chem. Eng.* **6** (2018) 10058–10068, <https://doi.org/10.1021/acssuschemeng.8b01405>.
- [10] S.S. Nair, J.Y. Zhu, Y. Deng, A.J. Ragauskas, *Sustain. Chem. Process.* **2** (2014), <https://doi.org/10.1186/s40508-014-0023-0>.
- [11] Z. Song, H. Xiao, Y. Zhao, *Carbohydr. Polym.* **111** (2014) 442–448, <https://doi.org/10.1016/j.carbpol.2014.04.049>.
- [12] J.M. Raquez, Y. Murena, A.L. Goffin, Y. Habibi, B. Ruelle, F. DeBuyl, P. Dubois, *Compos. Sci. Technol.* **72** (2012) 544–549, <https://doi.org/10.1016/j.compscitech.2011.11.017>.
- [13] L.C. Tomé, R.J.B. Pinto, E. Trovatti, C.S.R. Freire, A.J.D. Silvestre, C.P. Neto, A. Gandini, *Green Chem.* **13** (2011), <https://doi.org/10.1039/c0gc00545b>.
- [14] K.-Y. Lee, F. Quero, J.J. Blaker, C.A.S. Hill, S.J. Eichhorn, A. Bismarck, *Cellulose* **18** (2011) 595–605, <https://doi.org/10.1007/s10570-011-9525-z>.
- [15] D. Rigotti, R. Checchetto, S. Tarter, D. Carretti, M. Rizzuto, L. Fambri, A. Pegoretti, *Express Polym. Lett.* **13** (2019) 858–876, <https://doi.org/10.3144/expresspolymlett.2019.75>.
- [16] D. Rigotti, A. Pegoretti, A. Miotello, R. Checchetto, *Appl. Surf. Sci.* **507** (2020), <https://doi.org/10.1016/j.apsusc.2019.145066>.
- [17] D. Guangxi, L. Hongyu, C. Vicki, J. Mater. Chem. (2013) 4610–4630.
- [18] R. Checchetto, A. Miotello, L. Nicolais, G. Carotenuto, *J. Membr. Sci.* **463** (2014) 196–204.
- [19] P.N.P.D. Roilo, R.S. Brusa, A. Miotello, S. Aghion, R. Ferragut, R. Checchetto, *Polymer* **121** (2017) 17–25.
- [20] M.A. Aaron, A.F. Ismail, T. Matsuura, M.M. Montazer-Rahmati, *Separ. Purif. Technol.* **75** (2010) 229–242.
- [21] R.H.B. Bouma, A. Checchetti, G. Chidichimo, E. Drioli, *J. Membr. Sci.* **128** (1997) 141–149.
- [22] W. Egger, *Proceedings of the International School of Physics "Enrico Fermi"*, 2010.
- [23] R. Checchetto, *Int. J. Polym. Sci.* **2018** (2018) 1–9, <https://doi.org/10.1155/2018/4903904>.
- [24] Y.C. Jean, J.D. Van Horn, W.-S. Hung, K.-R. Lee, *Macromolecules* **46** (2013) 7133–7145, <https://doi.org/10.1021/ma401309x>.
- [25] W. Egger, P. Sperr, G. Kögel, G. Dollinger, *Phys. Status Solidi* **4** (2007) 3969–3972, <https://doi.org/10.1002/pssc.200675812>.
- [26] P. Sperr, W. Egger, G. Kögel, G. Dollinger, C. Hugenschmidt, R. Repper, C. Piochacz, *Appl. Surf. Sci.* **255** (2008) 35–38, <https://doi.org/10.1016/j.apsusc.2008.05.307>.
- [27] C. Hugenschmidt, G. Dollinger, W. Egger, G. Kögel, B. Löwe, J. Mayer, P. Pikart, C. Piochacz, R. Repper, K. Schreckenbach, P. Sperr, M. Stadlbauer, *Appl. Surf. Sci.* **255** (2008) 29–32, <https://doi.org/10.1016/j.apsusc.2008.05.304>.
- [28] C. Hugenschmidt, C. Piochacz, M. Reiner, K. Schreckenbach, *New J. Phys.* **14** (2012), <https://doi.org/10.1088/1367-2630/14/5/055027>.
- [29] A.F. Makhov, *Sov. Phys. Solid State* **2** (1961) 1942–1944.
- [30] J. Algers, P. Sperr, W. Egger, G. Kögel, F.H.J. Maurer, *Phys. Rev. B* **67** (2003), <https://doi.org/10.1103/PhysRevB.67.125404>.
- [31] M. Eldrup, D. Lightbody, J.N. Sherwood, *Chem. Phys.* **63** (1981) 51–58, [https://doi.org/10.1016/0301-0104\(81\)80307-2](https://doi.org/10.1016/0301-0104(81)80307-2).
- [32] S.J. Tao, *J. Chem. Phys.* **56** (1972) 5499–5510, <https://doi.org/10.1063/1.1677067>.
- [33] H. Nakanishi, S.J. Wang, Y.C. Jean, in: S.C. Sharma (Ed.), *In Positron Annihilation Studies of Fluids*, World Scientific, Singapore, 1988.
- [34] <http://palsfit.dk/>.
- [35] T. Merkel, I. Pinnau, R. Prabhakar, B. Freeman, in: Y. Yampolskii, I. Pinnau, B. Freeman (Eds.), *In Materials Science of Membranes for Gas and Vapor Separation*, Wiley, Chichester, 2006.
- [36] L. Bao, J.R. Dorgan, D. Knauss, S. Hait, N.S. Oliveira, I.M. Marucho, *J. Membr. Sci.* **285** (2006) 166–172, <https://doi.org/10.1016/j.memsci.2006.08.021>.
- [37] R. Auras, B. Harte, S. Selke, *Macromol. Biosci.* **4** (2004) 835–864, <https://doi.org/10.1002/mabi.200400043>.
- [38] D. Roilo, C.A. Maestri, M. Scarpa, P. Bettotti, W. Egger, T. Koschine, R.S. Brusa, R. Checchetto, *J. Phys. Chem. C* **121** (2017) 15437–15447, <https://doi.org/10.1021/acs.jpcc.7b02895>.
- [39] R. Checchetto, D. Rigotti, A. Pegoretti, A. Miotello, *Pure Appl. Chem.* **92** (2020) 391–398, <https://doi.org/10.1515/pac-2018-1216>.
- [40] H. Nakanishi, Y.C. Jean, E.G. Smith, T.C. Sandreczki, *J. Polym. Sci. B Polym. Phys.* **27** (1989) 1419–1424, <https://doi.org/10.1002/polb.1989.090270704>.
- [41] C. Wolf, H. Angellier-Coussy, N. Gontard, F. Doghieri, V. Guillard, *J. Membr. Sci.* **556** (2018) 393–418, <https://doi.org/10.1016/j.memsci.2018.03.085>.